

NuLite - Lightweight and Fast Model for Nuclei Instance Segmentation and Classification

Cristian Tommasino^{a,*}, Cristiano Russo^a, Antonio M. Rinaldi^a

^a*Department of Electrical Engineering and Information Technology University of Naples Federico II, Via Claudio, 21, Naples 80125, Italy*

Abstract

In pathology, accurate and efficient analysis of Hematoxylin and Eosin (H&E) slides is crucial for timely and effective cancer diagnosis. Although many deep learning solutions for nuclei instance segmentation and classification exist in the literature, they often entail high computational costs and resource requirements, thus limiting their practical usage in medical applications. To address this issue, we introduce a novel convolutional neural network, NuLite, a U-Net-like architecture designed explicitly on Fast-ViT, a state-of-the-art (SOTA) lightweight CNN. We obtained three versions of our model, NuLite-S, NuLite-M, and NuLite-H, trained on the PanNuke dataset. The experimental results prove that our models equal CellViT (SOTA) in terms of panoptic quality and detection. However, our lightest model, NuLite-S, is 40 times smaller in terms of parameters and about 8 times smaller in terms of GFlops, while our heaviest model is 17 times smaller in terms of parameters and about 7 times smaller in terms of GFlops. Moreover, our model is up to about 8 times faster than CellViT. Lastly, to prove the effectiveness of our solution, we provide a robust comparison of external datasets, namely CoNseP, MoNuSeg, and GlySAC. Our model is publicly available at <https://github.com/CosmoIknosLab/NuLite>.

Keywords:

2000 MSC: 68T45, 68T10, 68U07, 92C55 Nuclei segmentation, Computational pathology, Deep learning, Vision transformer

1. Introduction

Cancer is a disease concerned with the uncontrolled growth and spread of abnormal cells, a significant global health challenge [1]. Accurate diagnosis is essential in cancer treatment because it enables targeted therapies that improve patient outcomes and the chance of recovery. Advancements in computer vision techniques have significantly affected computational pathology (CPATH), opening new frontiers for analyzing histopathological images, like the Hematoxylin and Eosin (H&E) stained one [2]. The precise segmentation and classification of cells became an exciting task in the literature due to the importance of understanding the morphology and topology of tissue in cancer diagnosis [3]. However, this task in complex tissue environments poses many challenges due to the heterogeneity and overlap of nuclei structures, demanding robust and efficient solutions [4]. To address these challenges, recent research has focused on developing sophisticated algorithms that leverage deep learning techniques, demonstrating superior performance in various image analysis tasks. These algorithms are designed to accurately identify and classify cellular components, even in complex and heterogeneous tissue environments, thereby assisting pathologists in making more informed diagnostic decisions. Moreover, integrating machine learning models with domain-specific knowledge, such as the spatial relationships and morphological features of cells, has further en-

hanced the accuracy and robustness of computational pathology tools. This synergy between advanced computational methods and medical expertise promises to significantly advance the field of cancer diagnostics, offering the potential for more personalized and effective treatment plans.

Over the years, scholars have proposed many methods to overcome traditional barriers encountered in histopathological analysis in different tasks [5, 6]. In particular, many deep learning solutions have shown promising results for nuclei instance segmentation and classification tasks, starting with the introduction of U-Net [7]. Furthermore, advanced neural network architectures, like ResNet [8] and Vision Transformer (ViT) [9], offered sophisticated mechanisms for learning detailed features and patterns without the constraints imposed by prior techniques, further improving the effectiveness of new models. The recent trend toward integrating different modalities of deep learning, such as Convolutional Neural Networks (CNNs) combined with structures like U-Nets or multi-branch networks like HoVer-Net [10], demonstrates the field's evolution toward more precise and robust techniques. Additionally, implementing spatial and morphological constraints within network architectures further refine their output, ensuring that cell segmentation is precise and contextually appropriate. Moreover, a recent technique, CellViT [11], demonstrated using ViT to address nuclei instance segmentation and classification tasks, achieving the SOTA results.

In this manuscript, we present NuLite, a new UNet-like CNN [7] architecture designed explicitly for segmenting and classifying nuclei instances in Hematoxylin and Eosin (H&E) images. Our architecture consists of the FastViT [12] encoder with three

*Corresponding author

Email addresses: cristian.tommasino@unina.it (Cristian Tommasino), cristiano.russo@unina.it (Cristiano Russo), antoniomaria.rinaldi@unina.it (Antonio M. Rinaldi)

decoders, each purpose-built to perform one of the tasks identified in the HoVer-Net: nuclei prediction, horizontal and vertical map prediction, and nuclei classification [10]. NuLite is a faster, lighter alternative with state-of-the-art (SOTA) panoptic quality and detection performance. We proved its efficacy and efficiency through rigorous testing on benchmark datasets such as PanNuke [13]. Furthermore, we conducted comprehensive evaluations on additional datasets such as MoNuSeg [14], CoNSeP [10], and GlySAC [15]. NuLite consistently achieved SOTA results in these tests, outperforming advanced models like CellViT in various metrics, including precision, recall, and F1-score. These evaluations underscore the robustness and generalizability of NuLite across different types of histopathological images, highlighting its potential as a versatile tool in computational pathology.

Our main contributions to the field are significant regarding performance and its practical implications for enhancing diagnostic workflows. By enabling more accurate and efficient nuclei segmentation and classification, NuLite facilitates better quantitative analysis of tissue samples, which is crucial for improving diagnostic accuracy and patient outcomes in oncology and other medical disciplines.

We organized the rest of the paper as follows: Section 2 draws a brief state of the art about nuclei instance segmentation and vision transformer in pathology; Section 3 introduces our method, highlighting the architecture of the proposed CNN and loss function used to train it; Section 4 presents our experimental design and reports the experimental results with a comparison with SOTA and results on external datasets; lastly, Section 5 discusses the achieved results and Section 6 draws back the conclusions.

2. Related Works

This section introduces the literature that addresses the nuclei instance segmentation and classification task. Then, we briefly introduce vision transform (ViT) literature.

2.1. Nuclei Instance Segmentation

Over the years, numerous methods for nuclei instance segmentation have been proposed. The first challenge they tried to overcome was to separate the overlapped nuclei; then, they addressed the classification of nuclei. In the following, we report the main work related to traditional and deep learning methods.

2.1.1. Traditional methods

In fluorescence microscopy, Malpica et al. [16] proposed to use morphological watershed algorithms to effectively segment clustered nuclei, employing both gradient- and domain-based strategies to address the challenges of clustered nuclei segmentation. Similarly, Xiaodong Yang et al. [17] improved the tracking and analysis of nuclei in time-lapse microscopy via a marker-controlled watershed technique for initial segmentation, supplemented by mean-shift and Kalman filter techniques for dynamic and complex cellular behaviors. Likewise, Jierong

Cheng et al. [18] improved segmentation accuracy by introducing shape markers derived from an adaptive H-minima transform associated with a marking function based on the outer distance transform. Stephan Wienert et al. [19] involved a minimum-model strategy for the efficient detection and segmentation of cell nuclei in virtual microscopy images, simplifying the process while preserving effectiveness. Instead, in histopathological imaging, the study by Afaf Tareef et al. [20] introduced a multi-pass fast watershed method for accurate segmentation of overlapping cervical cells, using a novel three-pass process to segment both the nucleus and cytoplasm. Similarly, Miao Liao et al. [21] developed a method that utilizes bottleneck detection and ellipse fitting to segment overlapping cells accurately. Moreover, Sahirzeeshan Ali et al. [22] provided a solution for overlapping objects in histological images by integrating region-based, boundary-based, and shape-based active contour models, significantly enhancing the segmentation accuracy of closely adjacent structures. Instead, Veta et al. [23] employed a marker-controlled watershed technique incorporating a multiscale approach and multiple marker types to improve nucleus segmentation in H&E stained images for breast cancer histological images.

2.1.2. Deep learning approaches

In the last decade, deep learning techniques leveraged the limitations of traditional approaches. One of the first networks that achieved promising results in nuclei segmentation, posing the basis for all modern techniques, was U-Net proposed by Olaf Ronneberger et al. [7]. U-Net is an encoder-decoder neural network with skip connections, which helps preserve details crucial for medical image analysis. However, its original version proposed a way to separate clustered nuclei, which is a significant challenge in histopathology. Another network was BRP-Net [24] that creates nuclei proposals in the first place, then refines the boundary, and finally creates a segmentation out of this. However, this approach resulted in computationally intensive and slow. Similarly, Alemi et al. introduced Mask-RCNN [25], built on Fast-RCNN [26], adding a segmentation branch after nuclei detection. Instead, Raza et al. proposed Micro-Net [27] updating U-Net to handle nuclei of varying sizes. Another network that significantly improved the nuclei instance segmentation and classification is HoVer-Net [10], which has U-Net architecture with three branches that predict nuclei against the background, vertical and horizontal map, and nuclei types. The vertical and horizontal maps are crucial to separate overlapped nuclei and, in general, to perform instance segmentation. Following the idea of [10], the authors in [11] proposed CellViT, which follows the same architecture but employs a ViT as the encoder, and the authors designed a decoder inspired by UNETR [28]. Instead, authors in [29] proposed a framework to obtain a smaller and lighter model than HoVerNet, HoVer-UNet, that is, a U-Net-like neural network with one decoder trained using a knowledge distillation approach. Other recent networks proposed in the literature are STARDIST [30] and CPP-Net [31], which used star-convex polygons for segmentation, with CPP-Net enhancing the model by integrating shape-aware loss functions to improve accuracy. Similarly,

TSFD-Net [32] employed a Feature Pyramid Network and integrated a tissue-classifier branch to handle tissue-specific features, using advanced loss functions to manage class imbalance. Moreover, the SONNET [15] network is a deep learning model designed for simultaneous segmentation and classification of nuclei in large-scale multi-tissue histology images. It employs a self-guided ordinal regression approach that stratifies nuclear pixels based on their distance from the center of mass, improving the accuracy of segmenting overlapping nuclei.

2.2. Vision Transformers

Vision Transformers (ViTs) have revolutionized image segmentation by providing advanced encoder-decoder architectures that enhance the capabilities of traditional U-Net-based models. Incorporating ViTs into these frameworks has enabled more precise instance and semantic segmentation across various domains, including medical imaging. TransUNet [33] leverages a transformer to encode tokenized patches from CNN feature maps, effectively incorporating global context within the segmentation process. SETR [34] uses the original ViT as the encoder and a fully convolutional network as the decoder, connected without intermediate skip connections, simplifying the architecture while maintaining performance. UNETR [28] combining a standard ViT with a U-Net-like decoder that includes skipping connections, this model has shown to outperform others like TransUNet and SETR in medical image segmentation, demonstrating the effectiveness of integrating pre-trained ViTs with conventional segmentation networks. Pre-training ViTs on large datasets is crucial for their success in segmentation tasks. Unlike CNNs, ViTs lack certain inductive biases and thus require substantial training data to learn effective representations. This is especially significant in medical imaging, where annotated data is limited. Self-supervised pre-training methods, such as DINO [35], have been pivotal in using unlabeled data to prime ViTs for fine-tuning specific segmentation tasks. Xie et al. introduced Segformer [36], a model that utilizes a transformer as an image encoder coupled with a lightweight MLP decoder, focusing on efficiency and scalability. FastViT [12] is a high-speed hybrid vision transformer model that effectively balances latency and accuracy. It introduces a novel RepMixer component to reduce memory costs and enhance processing speed, making it faster and more efficient than traditional models across various image processing tasks.

3. Methods

This section introduces NuLite architecture, the loss function used to train it, and the post-processing function. Lastly, we detail the inference pipeline.

3.1. NuLite architecture

We designed NuLite with a U-Net-like architecture and three decoders, utilizing FastViT [12], a state-of-the-art Vision Transformer known for its lightweight and efficient design as the backbone. The decision to use a U-Net structure is based on

its proven success in medical image segmentation tasks, which aligns with our goal of accurate nuclei detection and classification. Our approach draws inspiration from HoVer-Net [10], which has established itself in the literature as an effective method for nuclei segmentation. Therefore, our model predicts nuclei maps, type maps, and horizontal and vertical maps, followed by a watershed algorithm to perform nuclei instance segmentation in a postprocessing step. Thus, our network comprises three specialized decoders: the NP-BRANCH for nuclei segmentation against the background, the HV-BRANCH for predicting horizontal and vertical orientation maps, and the NC-BRANCH for nuclei classification, as illustrated in Figure 1. This architecture supports detailed nuclei analysis through a postprocessing step that leverages the NP-BRANCH and HV-BRANCH outputs to precisely detect individual nuclei, subsequently using the NC-BRANCH for classification. We carefully designed the decoders to minimize computational overhead, maintaining low parameter counts and GFlops, thus ensuring efficiency. Furthermore, we integrated a dense layer within the encoder to facilitate tissue classification, extending the functionality of the network beyond nuclei analysis, and results useful during the training step to improve the segmentation and classification capabilities. We focused on the decoder design, and we built it to work with the FastViT encoder. Therefore, the decoder consists of six main layers, as detailed in Table 1. As a standard U-like architecture, we designed the skip con-

Table 1: NuLite decoder details

#Layer	Layer composition	Input Shape	Output shape
1	Conv2D (3x3) - BN - ReLU DeConv (2x2)	$8 \cdot Z \times \frac{H}{32} \times \frac{W}{32}$	$4 \cdot Z \times \frac{H}{16} \times \frac{W}{16}$
2	Conv2D (3x3) - BN - ReLU Conv2D (3x3) - BN - ReLU DeConv (2x2)	$8 \cdot Z \times \frac{H}{16} \times \frac{W}{16}$	$2 \cdot Z \times \frac{H}{8} \times \frac{W}{8}$
3	Conv2D (3x3) - BN - ReLU Conv2D (3x3) - BN - ReLU DeConv (2x2)	$4 \cdot Z \times \frac{H}{8} \times \frac{W}{8}$	$Z \times \frac{H}{4} \times \frac{W}{4}$
4	Conv2D (3x3) - BN - ReLU DeConv (2x2)	$2 \cdot Z \times \frac{H}{4} \times \frac{W}{4}$	$Z \times \frac{H}{2} \times \frac{W}{2}$
5	Conv2D (3x3) - BN - ReLU DeConv (2x2)	$Z \times \frac{H}{2} \times \frac{W}{2}$	$Z \times H \times W$
6	Conv2D (3x3) - BN - ReLU Conv2D (1x1)	$2 \cdot Z \times H \times W$	$C \times H \times W$

nnection between the main block output of the encoder, namely stage 1 to stage 4, as shown in Figure 1, and each main block of our branches. Furthermore, we added a skip connection between the original output after a convolutional layer and the last layer of each decoder. The architecture of each decoder comprises six functional layers, as described in Table 1. These layers operate on input images defined by dimensions height H and width W , with Z indicating the number of channels from the encoder. The first, fourth, and fifth layers are structured with a 3×3 convolutional layer, which is succeeded by batch normalization and ReLU activation and augmented by a deconvolution layer. The output from the first and fourth layers yields feature maps with half the number of channels of Z but with dimensions expanded to twice the height ($2H$) and width ($2W$). The fifth layer, however, maintains the channel count of Z and dou-

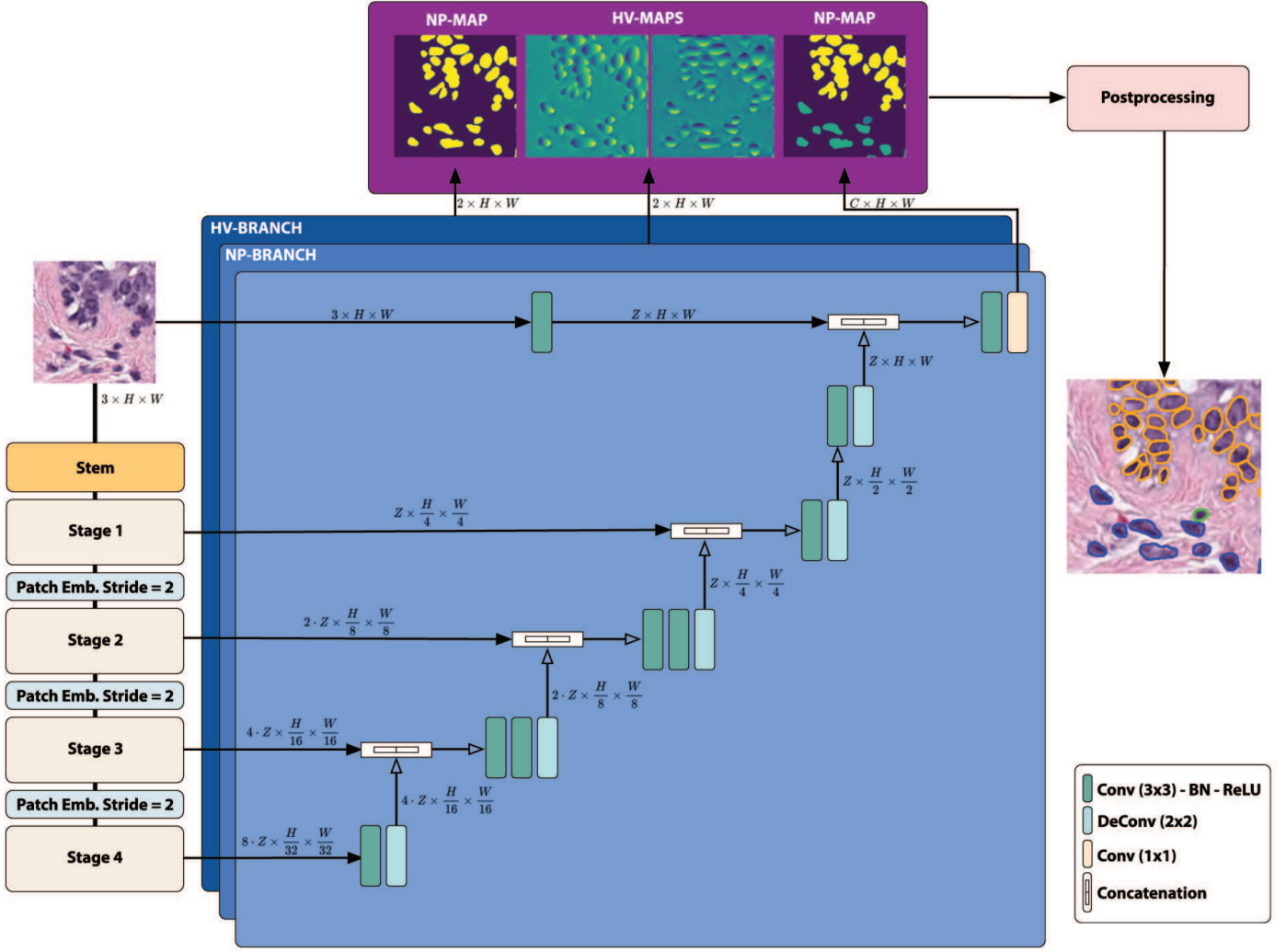


Figure 1: NuLite architecture. The network takes as input multiple feature maps, each encoding different spatial and contextual information. These features are then processed through convolutional and pooling layers, organized into distinct stages and branches. The network employs patch embedding to capture local patterns and leverages deconvolutional layers to generate a high-resolution segmentation map. The final output is a pixel-wise classification that assigns each pixel to a specific tissue class.

bles the height and width. The design of the second and third layers integrates two 3×3 convolutional layers, each followed by batch normalization and ReLU activation. These layers are completed by a deconvolution layer that produces outputs with a quarter of the channels of Z and twice the original dimensions in height and width. The final, sixth layer includes a 3×3 convolution followed by batch normalization and ReLU, culminating in a 1×1 convolution that adjusts the output channels to meet specific requirements. As notable from the decoder structure, the second and third layers contain two convolutional blocks, while the rest have only one convolutional block. That is because the number of feature maps is reduced by 4 times in the second and third and 2 times in the rest. FastViT exists in several configurations, distinguished by their specifications. The available variants include T8, T12, S12, SA12, SA24, SA36, and MA36. The parameter Z , which denotes the number of channels, varies across these models. Specifically, Z is set to 384 for T8, while it remains consistent at 512 for T12, S12, SA12, SA24, and

SA36. For the MA36 configuration, Z increases to 608. Therefore, in this paper, we consider a server version of NuLite, each using a version of FastViT.

3.2. Loss function

To train NuLite, we use a combination of different loss functions for each network branch, as also suggested in [10, 11]. Therefore, the total loss is defined as the sum of a loss for each branch, as shown in Equation 1.

$$L_{\text{total}} = L_{NP} + L_{HV} + L_{NT} + L_{TC} \quad (1)$$

L_{NP} is the loss for the NP-branch, defined as a linear combination of Focal Tversky loss (FTL) and Dice loss (DICE), as shown in Equation 2.

$$L_{NP} = \lambda_{NP}^{\text{FTL}} L_{\text{FTL}} + \lambda_{NP}^{\text{DICE}} L_{\text{DICE}} \quad (2)$$

L_{HV} is the loss for the HV-branch, defined as a linear combination of Mean Square Error (MSE) and Mean Square Gradient

Error (MSGE), as shown in Equation 3.

$$L_{HV} = \lambda_{HV}^{\text{MSE}} L_{\text{MSE}} + \lambda_{HV}^{\text{MSGE}} L_{\text{MSGE}} \quad (3)$$

L_{NT} is the loss for the NT-branch, defined as a linear combination of FLT, DICE, and Binary Cross Entropy Loss (BCE) as shown in Equation 4.

$$L_{NT} = \lambda_{NT}^{\text{FLT}} L_{\text{FLT}} + \lambda_{NT}^{\text{DICE}} L_{\text{DICE}} + \lambda_{NT}^{\text{BCE}} L_{\text{BCE}} \quad (4)$$

L_{TC} the loss for the TC-branch, computed as Cross Entropy (CE) as shown in Equation 5

$$L_{TC} = \lambda_{TC}^{\text{CE}} L_{\text{CE}} \quad (5)$$

In these equations, $\lambda_{\text{branch}}^{\text{loss}}$ coefficients represent the weight given to each loss component within a branch.

3.3. Post-Processing

As described in the preview sections, our network, NuLite, encloses three specialized branches dedicated to extracting essential information for a nuclei instance segmentation and classification postprocessing step. Due to our network following the idea proposed in HoVer-Net and Cell-ViT, postprocessing is a crucial step in refining the raw predictions produced by the network. NP-BRANCH output is a probability map indicating the likelihood of each pixel belonging to a nucleus. A threshold is applied to this probability map to generate a binary mask. Pixels with probabilities above the threshold are considered part of a nucleus. HV-BRANCH contains horizontal and vertical gradient maps (HV maps) that help to delineate the nuclei boundaries more accurately. These maps provide additional information about the direction and magnitude of changes in the image, which is useful for refining the edges of the segmented nuclei. The gradient information from the HV maps is used to split merged nuclei. This process is critical when there are overlapped nuclei. Each nucleus identified from the segmentation step is classified according to the output of TP-BRANCH. Finally, some morphological operations, like dilation and erosion, can be applied to smooth the boundaries of the segmented nuclei and remove small noise artifacts, improving the visual quality of the segmentation masks.

4. Experimental Results

This section introduces the dataset employed, the metrics used to evaluate our network, the training details, and the experimental results with a related comparison with SOTA on the PanNuke dataset. Lastly, we comprehensively analyze inference time and network complexity and show the results on another external dataset.

4.1. Datasets

PanNuke. The PanNuke dataset is the primary resource for training and evaluating our model. It comprises 189,744 annotated nuclei across 7,904 images, each of size 256×256 pixels, spanning 19 distinct tissue types and categorized into five

unique cell classes. These cell images were captured at a 40× magnification with a fine resolution of 0.25 $\mu\text{m}/\text{px}$. Notably, the dataset exhibits a significant class imbalance; particularly, the nuclei class of dead cells is markedly underrepresented, evident from the nuclei and tissue class statistics.

MoNuSeg. The MoNuSeg dataset is employed as a supplementary resource for nuclei segmentation. Unlike PanNuke, MoNuSeg is considerably smaller and does not categorize nuclei into various classes. In this study, only the test subset of MoNuSeg is used to assess our model. This subset includes 14 high-resolution images (1000 × 1000 px) captured at 40× magnification and a resolution of 0.25 $\mu\text{m}/\text{px}$, containing over 7,000 annotated nuclei spanning seven organ types (kidney, lung, colon, breast, bladder, prostate, and brain) across various disease states. Due to the absence of nuclei labels, classification performance cannot be evaluated with this dataset.

CoNSeP. The CoNSeP dataset, curated by Graham et al., comprises 41 H&E-stained colorectal adenocarcinoma whole slide images (WSIs) at a resolution of 0.25 $\mu\text{m}/\text{px}$, resized to 1024 × 1024 px to facilitate processing. This diverse dataset features stromal, epithelial, muscular, collagen, adipose, and tumorous regions. It also includes a variety of nuclei types derived from different originating cells, such as normal epithelial, dysplastic epithelial, inflammatory, necrotic, muscular, fibroblast, and miscellaneous nuclei types, including necrotic and mitotic cells, which aids in comprehensive phenotypic analysis.

GlySAC. The GLySAC dataset, short for Gastric Lymphocyte Segmentation and Classification, focuses on segmenting and classifying nuclei within gastric pathology. It contains 59 H&E stained image tiles, each 1000x1000 pixels, sourced from gastric adenocarcinoma WSIs and captured at a 40× magnification using an Aperio digital scanner. The dataset encapsulates a total of 30,875 nuclei, categorized into three primary groups: Lymphocytes (12,081 nuclei), Epithelial nuclei (12,287 nuclei), encompassing both cancerous and normal cells, and Miscellaneous other nuclei types (6,507 nuclei).

4.2. Evaluation metrics

In evaluating nuclear instance segmentation, traditional metrics such as the Dice coefficient and Jaccard index often fall short as they do not adequately reflect the detection quality of individual nuclei or the precision in segmenting overlapping nuclei. Therefore, more sophisticated metrics are employed as suggested in [10, 11, 15, 32].

Panoptic Quality.

$$DQ = \frac{|TP|}{|TP| + \frac{1}{2}|FP| + \frac{1}{2}|FN|} \quad (6)$$

SQ assesses the accuracy of the segmentation for the detected nuclei, computed as the mean IoU (Intersection over Union) of matched segments, as denoted in Equation 7, where y and \hat{y} denote the ground truth and predicted segments, respectively.

$$SQ = \frac{\sum_{(y, \hat{y}) \in TP} IoU(y, \hat{y})}{|TP|} \quad (7)$$

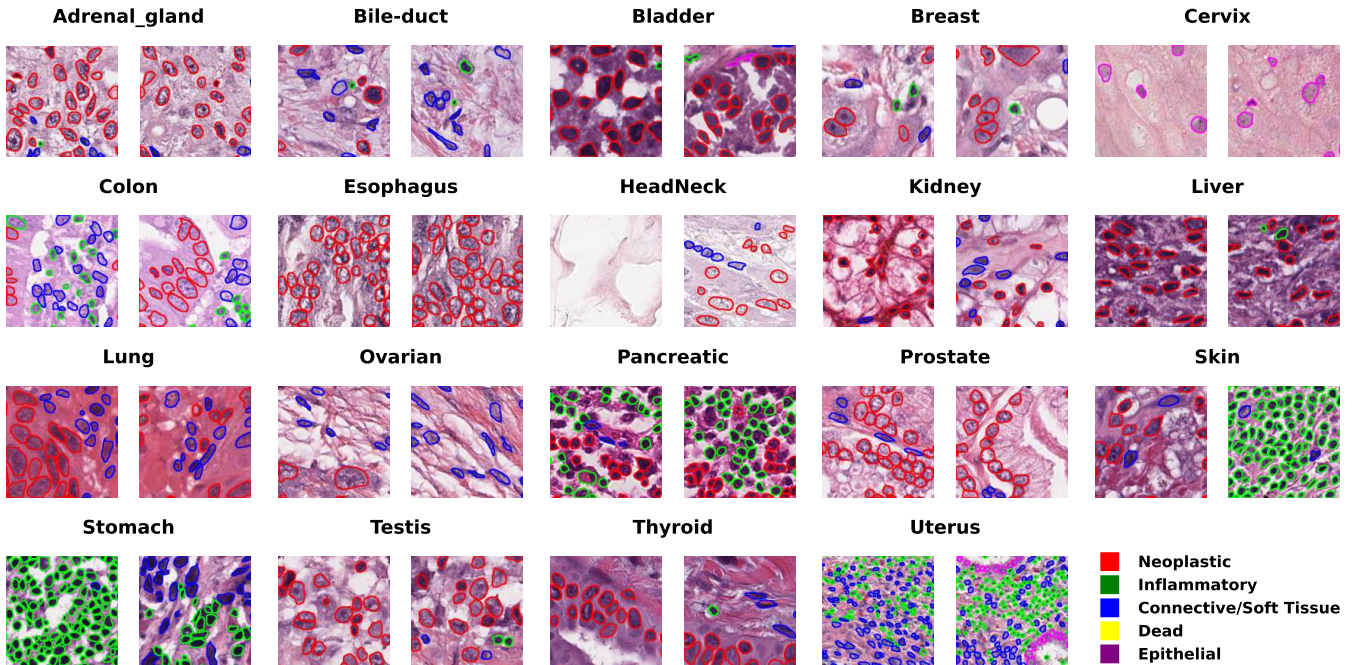


Figure 2: Example images from the PanNuke dataset showing varied tissue types and nuclear annotations.

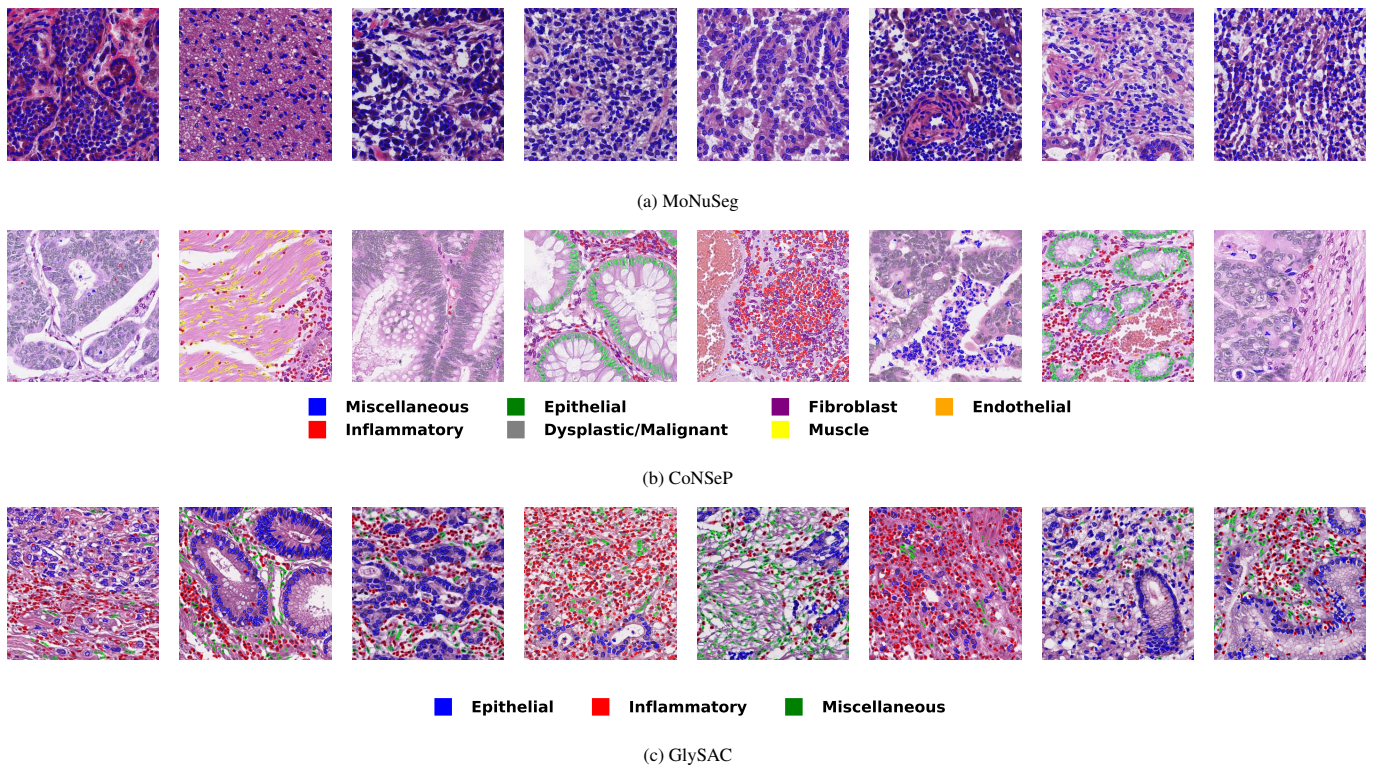


Figure 3: Examples images from MoNuSeg, CoNSeP, and GlySAC dataset with annotations

Therefore, panoptic quality is definite as the product of detection quality and segmentation quality as denoted in equation 8.

$$PQ = DQ \times SQ \quad (8)$$

In this work, we consider two adaptions of PQ: Binary PQ (bPQ), which considers all nuclei as a single class against the background, and Multi-class PQ (mPQ), which Evaluates PQ separately for each class of nuclei and averages the scores.

F1-score. Several metrics commonly utilized in machine learning were employed to evaluate our model’s classification performance. Precision (P), which quantifies the accuracy of the model’s positive predictions, is defined in the equation environment as follows:

$$P = \frac{TP}{TP + FP} \quad (9)$$

where TP represents true positives and FP stands for false positives. Recall (R), also known as sensitivity, measures the ability of the model to detect all relevant instances encapsulated by:

$$R = \frac{TP}{TP + FN} \quad (10)$$

with FN indicating false negatives. The F1 Score, a harmonic mean of precision and recall that provides a balance between these metrics, is crucial in the presence of uneven class distribution and is expressed by:

$$F1 = 2 \times \frac{P \times R}{P + R} \quad (11)$$

Accuracy, indicating the overall correctness of the model, is formulated as:

$$Accuracy = \frac{TP + TN}{TP + TN + FP + FN} \quad (12)$$

where TN represents true negatives.

To accommodate detailed performance assessment in multi-class settings, the F1 Score is further refined through equations that include terms for each class c and d , illustrating both traditional components and inter-class effects:

$$F1_c = \frac{2(T_{Pc} + T_{Nc})}{2(T_{Pc} + T_{Nc}) + 2FP_c + 2FN_c + FP_d + FN_d} \quad (13)$$

$$P_c = \frac{T_{Pc} + T_{Nc}}{T_{Pc} + T_{Nc} + 2FP_c + FP_d} \quad (14)$$

$$R_c = \frac{T_{Pc} + T_{Nc}}{T_{Pc} + T_{Nc} + 2FN_c + FN_d} \quad (15)$$

These refinements enable a more comprehensive evaluation of the model discriminatory capacity between classes, essential in contexts where class imbalance or differential inter-class errors significantly impact performance.

4.3. Results on PanNuke

In this subsection, we detail the training strategy used to train NuLite on PanNuke and show its experimental results compared to similar methods.

Training. We used the AdamW optimizer for the training set, configured with specific hyperparameters, including beta values of 0.85 and 0.95, a learning rate of 0.0003, and a weight decay of 0.0001. An exponential scheduler managed the learning rate decay with a gamma of 0.85, effectively adjusting the learning rate across the epochs. Furthermore, we trained the model with a batch size 16 for 130 epochs. We used data augmentation techniques to ensure the model generalized well across

different imaging conditions. We employed geometric transformations, including rotations, flips, elastic transformations, simulated cell orientations, and position variations; photometric transformations, including blur, Gaussian noise, color jitter, and superpixel augmentation; and enhanced robustness against variations in stain quality and imaging noise. Lastly, we used a specific sampling strategy focusing on cell and tissue types, ensuring a balanced representation of various classes in the training batches, as shown in [11].

Table 2: Average PQ across the three PanNuke splits for each nucleus type on the PanNuke dataset. The best results are highlighted in bold, with the second-best in underlined text.

Model	Neoplastic	Epithelial	Inflammatory	Connective	Dead
DIST	0.439	0.29	0.343	0.275	0.000
Mask-RCNN	0.472	0.403	0.290	0.300	0.069
Micro-Net	0.504	0.442	0.333	0.334	0.051
HoVer-Net	0.551	0.491	0.417	0.388	0.139
HoVer-UNet	0.524	0.478	0.401	0.379	0.076
CellViT256	0.567	0.559	0.405	0.405	0.144
CellViT-SAM-H	0.581	0.583	0.417	0.423	0.149
NuLite-T	0.567	0.562	<u>0.418</u>	0.401	0.155
NuLite-M	<u>0.577</u>	0.561	0.422	0.409	0.151
NuLite-H	<u>0.577</u>	<u>0.566</u>	0.415	<u>0.412</u>	<u>0.153</u>

Training Results. We used the PanNuke dataset to evaluate the performance of our models on nuclei instance segmentation and classification of five distinct cell types: neoplastic, epithelial, inflammatory, connective, and dead cells. We consider the PQ and F-score for each nuclei type and the F-score for detection to perform a robust analysis. Furthermore, we compare our results with DIST, MASK-RCNN, MICRO-Net, HoVer-UNet, CellViT256, and CellViT-SAM-H. In the following results, we consider three NuLite versions: NuLite-T, NuLite-M, and NuLite-H, which respectively use FastViT-T12, FastViT-SA12, and FastViT-SA36 as encoders and, in inference, they are reparameterized as described in [12]. In the ablation study section, we justify the selected encoders and reparameterization. To compare our model with others, we take into account three aspects. First, we analyze the PQ for each nucleus type, reported in 2, then we analyze the F1-score, reported in Table 3. Lastly, we analyze the results regarding binary Panoptic Quality (bPQ) and multi-class Panoptic Quality (mPQ) over each tissue. All results are an average of over three training sessions, as the authors’ dataset suggested. PQ results show that our model is almost the second best and, in the case of inflammatory nuclei, is the best. Furthermore, the results for the different versions of NuLite are pretty similar. Again, analyzing the results in terms of the F1-score, reported in Table 3, NuLite achieves results practically equal to CellViT and outperforms other methods. Lastly, we compare the results over tissues, reported in Table 4, in terms of binary Panoptic Quality (bPQ) and multi-class Panoptic Quality (mPQ). These results prove that our NuLite is practically equal to CellViT-SAM-H, the best model, but more complex and slow than ours, as demonstrated in the following. Moreover, our models outperform CellViT256, the fastest version in the SOTA. In the model complexity analysis paragraph, we discuss the efficiency of NuLite in terms of parameters and

Table 3: Precision (P), Recall (R), and F1-score (F1) across the three PanNuke splits for binary detection and each nucleus type. The best results are highlighted in bold, with the second-best in underlined text.

Model	Detection			Classification														
				Neoplastic			Epithelial			Inflammatory			Connective			Dead		
	P	R	F1	P	R	F1	P	R	F1	P	R	F1	P	R	F1	P	R	F1
DIST	0.74	0.71	0.73	0.49	0.55	0.5	0.38	0.33	0.35	0.42	0.45	0.42	0.42	0.37	0.39	0	0	0
Mask-RCNN	0.76	0.68	0.72	0.55	0.63	0.59	0.52	0.52	0.52	0.46	0.54	0.5	0.42	0.43	0.42	0.17	0.3	0.22
Micro-Net	0.78	0.82	0.8	0.59	0.66	0.62	0.63	0.54	0.58	0.59	0.46	0.52	0.5	0.45	0.47	0.23	0.17	0.19
HoVer-Net	0.82	0.79	0.8	0.58	0.67	0.62	0.54	0.6	0.56	0.56	0.51	<u>0.54</u>	0.52	0.47	0.49	0.28	<u>0.35</u>	0.31
HoVer-UNet	0.8	0.79	0.79	0.59	0.69	0.64	0.57	0.67	0.62	0.55	0.52	0.53	0.52	0.45	0.48	0.21	0.16	0.18
CellViT256	<u>0.83</u>	0.82	<u>0.82</u>	<u>0.69</u>	<u>0.70</u>	0.69	0.68	0.71	0.70	0.59	0.58	0.58	0.53	<u>0.51</u>	<u>0.52</u>	0.39	<u>0.35</u>	<u>0.37</u>
CellViT-SAM-H	0.84	<u>0.81</u>	0.83	<u>0.72</u>	0.69	0.71	0.72	0.73	0.73	0.59	<u>0.57</u>	0.58	0.55	<u>0.52</u>	<u>0.53</u>	0.43	0.32	0.36
NuLite-T	0.82	0.82	<u>0.82</u>	0.68	0.71	0.69	0.70	<u>0.72</u>	0.71	0.57	0.58	0.58	0.54	0.49	<u>0.52</u>	0.39	0.36	0.38
NuLite-M	<u>0.83</u>	0.82	<u>0.82</u>	<u>0.69</u>	0.71	<u>0.70</u>	0.72	<u>0.72</u>	<u>0.72</u>	<u>0.58</u>	0.58	0.58	0.55	0.50	<u>0.52</u>	0.38	<u>0.35</u>	0.36
NuLite-H	0.82	0.82	<u>0.82</u>	<u>0.69</u>	0.71	<u>0.70</u>	<u>0.71</u>	<u>0.72</u>	<u>0.72</u>	0.59	0.58	0.58	0.53	<u>0.52</u>	<u>0.52</u>	<u>0.40</u>	0.34	<u>0.37</u>

Table 4: Multi-class Panoptic Quality (mPQ) and binary Panoptic Quality (bPQ) across the three PanNuke splits over tissues among HoVerNet, CellViT, and NuLite. The best results are highlighted in bold, with the second-best in underlined text.

Tissue	HoVer-Net		CellViT256		CellViT-SAM-H		NuLite-T12		NuLite-SA24		NuLite-SA36	
	mPQ	bPQ	mPQ	bPQ	mPQ	bPQ	mPQ	bPQ	mPQ	bPQ	mPQ	bPQ
Adrenal	0.481	0.696	0.495	0.701	0.513	<u>0.709</u>	0.479	0.703	0.498	0.716	0.490	0.715
Bile Duct	0.471	0.670	0.472	0.671	0.489	<u>0.678</u>	0.472	0.671	0.482	<u>0.676</u>	0.482	0.678
Bladder	0.579	0.703	0.576	0.706	<u>0.584</u>	0.707	0.570	0.700	0.592	<u>0.721</u>	<u>0.580</u>	0.709
Breast	0.490	0.647	0.509	0.664	0.518	<u>0.675</u>	0.508	0.662	0.511	<u>0.666</u>	0.516	0.666
Cervix	0.444	0.665	0.489	0.686	0.498	<u>0.687</u>	0.486	0.685	0.505	<u>0.692</u>	0.491	<u>0.692</u>
Colon	0.410	0.558	0.425	0.570	0.449	<u>0.592</u>	0.435	0.573	<u>0.440</u>	0.579	0.440	0.582
Esophagus	0.509	0.643	0.537	0.662	<u>0.545</u>	<u>0.668</u>	0.535	0.665	<u>0.544</u>	0.675	0.543	0.672
Head & Neck	0.453	0.633	<u>0.490</u>	0.647	0.491	<u>0.654</u>	0.489	0.647	0.487	0.648	0.491	0.650
Kidney	0.442	0.684	0.541	0.699	<u>0.537</u>	0.709	0.540	0.699	0.531	0.702	0.530	0.703
Liver	0.497	0.725	0.507	0.716	0.522	<u>0.732</u>	0.516	0.727	<u>0.520</u>	<u>0.734</u>	0.516	0.735
Lung	0.400	0.630	0.410	0.632	0.431	<u>0.643</u>	0.400	0.640	0.410	0.649	0.412	0.647
Ovarian	0.486	0.631	0.526	0.660	0.539	<u>0.672</u>	<u>0.531</u>	0.664	<u>0.529</u>	<u>0.669</u>	0.528	0.672
Pancreatic	0.460	0.649	0.477	0.664	0.472	0.666	0.480	<u>0.669</u>	<u>0.496</u>	<u>0.674</u>	0.501	0.680
Prostate	0.510	0.662	0.516	0.670	0.532	<u>0.682</u>	0.512	<u>0.669</u>	0.511	<u>0.678</u>	0.528	0.682
Skin	0.343	0.623	0.366	0.640	0.434	<u>0.657</u>	0.395	0.641	<u>0.402</u>	0.644	<u>0.409</u>	0.646
Stomach	0.473	0.689	0.448	0.692	<u>0.471</u>	<u>0.702</u>	0.446	0.699	0.469	0.699	0.457	0.705
Testis	0.475	0.689	0.509	0.688	<u>0.513</u>	<u>0.696</u>	0.497	0.683	0.520	0.694	<u>0.511</u>	0.697
Thyroid	0.432	0.698	0.441	0.704	0.452	<u>0.715</u>	<u>0.449</u>	0.703	<u>0.450</u>	0.714	0.442	0.716
Uterus	0.439	0.639	0.474	0.652	<u>0.474</u>	<u>0.663</u>	0.457	0.650	<u>0.475</u>	0.661	0.492	0.665
Average	0.463	0.660	0.485	0.670	0.498	<u>0.679</u>	0.484	0.671	<u>0.493</u>	<u>0.679</u>	<u>0.493</u>	0.680
STD	0.050	0.038	0.050	<u>0.034</u>	0.041	<u>0.032</u>	0.046	<u>0.034</u>	0.046	0.035	<u>0.045</u>	<u>0.034</u>

the number of multiple additions, proving that it is the fastest and lightest SOTA. Lastly, we also compared our versions with CellViT over tissue types, as shown in Table 4. Again, these results demonstrate that NuLite in all its versions is similar to CellViT in binary panoptic quality (bPQ) and multi-class panoptic quality (mPQ). Therefore, these results show that using NuFastViT-H, we obtain the same results of CellViT-SAM-H in terms of PQ and F1-score, except for Epithelial nuclei. Also, considering a tiny version of NuLite, the results are not different from CellViT-SAM-H and are better or equal to CellViT256, which is the lightest version of it.

4.4. Ablation study

In this section, we describe the methodology used for selecting our models. We evaluated our NuLite using all versions of FastViT, considering both reparameterized and non-reparameterized variants during the inference phase. The results, as shown in Table 5, indicate that reparameterization does not significantly defect performance. Consequently, we opted for the reparameterized versions due to their superior computational efficiency, as demonstrated in Table 6. To provide a comprehensive representation, we selected three versions of NuLite, namely NuLite-T, NuLite-M, and NuLite-H, corresponding to tiny, medium, and large configurations, respectively. This selection was informed by the evaluation results on the PanNuke dataset, detailed in Table 5. The metrics used for evaluation in-

Table 5: Comparison between NuLite using reparameterized or no-reparameterized FastViT as an encoder in terms of binary panoptic quality (bPQ), multiclass panoptic quality (mPQ), PQ for each nucleus type, F1-score, and F1-score for each nucleus type.

Encoder	Binary			Multi-Class					F1-score					
	bPQ	mPQ	F1	Panoptic Quality					F_1^N	F_1^E	F_1^I	F_1^C	F_1^D	
				PQ^N	PQ^E	PQ^I	PQ^C	PQ^D						
No Reparameterized	FastViT-T8	0.6520	0.4808	0.8211	0.5668	0.5512	0.4196	0.3967	0.1479	0.6902	0.7033	0.5788	0.5164	0.3719
	FastViT-T12	0.6546	0.4825	0.8225	0.5666	0.5612	0.4183	0.4009	0.1536	0.6910	0.7084	0.5764	0.5173	0.3756
	FastViT-S12	0.6550	0.4862	0.8227	0.5719	0.5600	0.4241	0.4055	0.1354	0.6944	0.7073	0.5806	0.5176	0.3585
	FastViT-SA12	0.6576	0.4874	0.8228	0.5732	0.5575	0.4243	0.4065	0.1417	0.6914	0.7040	0.5837	0.5218	0.3604
	FastViT-SA24	0.6610	0.4893	0.8246	0.5773	0.5597	0.4215	0.4087	0.1504	0.6989	0.7193	0.5798	0.5216	0.3627
	FastViT-SA36	0.6620	0.4900	0.8246	0.5764	0.5661	0.4147	0.4123	0.1526	0.7010	0.7183	0.5793	0.5247	0.3657
	FastViT-MA36	0.6621	0.4912	0.8254	0.5779	0.5732	0.4199	0.4119	0.1442	0.7005	0.7249	0.5809	0.5261	0.3540
Reparameterized	FastViT-T8	0.6520	0.4810	0.8215	0.5671	0.5514	0.4194	0.3970	0.1470	0.6904	0.7035	0.5782	0.5165	0.3719
	FastViT-T12	0.6548	0.4827	0.8225	0.5667	0.5615	0.4183	0.4011	0.1545	0.6911	0.7084	0.5768	0.5176	0.3760
	FastViT-S12	0.6551	0.4864	0.8228	0.5718	0.5606	0.4244	0.4056	0.1361	0.6944	0.7075	0.5809	0.5177	0.3593
	FastViT-SA12	0.6575	0.4873	0.8227	0.5732	0.5567	0.4241	0.4064	0.1406	0.6913	0.7037	0.5840	0.5221	0.3606
	FastViT-SA24	0.6611	0.4895	0.8245	0.5772	0.5606	0.4217	0.4086	0.1505	0.6990	0.7192	0.5791	0.5216	0.3629
	FastViT-SA36	0.6621	0.4901	0.8247	0.5766	0.5658	0.4148	0.4123	0.1529	0.7009	0.7184	0.5796	0.5244	0.3664
	FastViT-MA36	0.6622	0.4913	0.8253	0.5781	0.5732	0.4201	0.4117	0.1429	0.7006	0.7248	0.5810	0.5263	0.3533

cluded binary panoptic quality (PQ), multi-class panoptic quality (mPQ), F1-score, panoptic quality, and F1-score for each nucleus type in the PanNuke dataset. The nucleus types are denoted as Neoplastic (N), Epithelial (E), Inflammatory (I), Connective/Soft Tissue (C), and Dead (D). Upon analyzing the results for the reparameterized models, it is apparent that the performance metrics are closely aligned across most variants. Thus, model selection also considered inference time and model complexity, as detailed in Table 6. First, we exclude the results with FastViT-T8 and FastViT-MA36; the first because despite being the lightest, the results are the worst; the second, because despite being the heaviest, the results are not enough better than the second heaviest model. Then, we chose FastViT-T12 as the backbone for NuLite-T due to its minimal parameter count, FastViT-SA24 as the backbone of NuList-M because it offers a balanced number of parameters and computational complexity without a substantial performance trade-off compared to larger models, and FastViT-SA36 for NuLite-H.

4.5. Models complexity analysis

To prove that our model, NuLite, has a lower complexity than CellViT, in Table 6, we report an exhaustive comparison between NuLite and CellViT in terms of parameters count and GFlops, estimated size, and latency on GPU using an input shape of 256 and 1024. In particular, we consider all FastViT models (T8, T12, S12, SA24, SA36, and MA36) and the reparameterized versions. Instead, for CellViT, we use the version with ViT256, SAM-B, SAM-L, and SAM-H as encoders. Results concerning GFlops and estimated size refer to a batch with just one image. Instead, GPU latency refers to a batch size of 4, and we repeated the experiments 100 times and reported the mean and variance in milliseconds. We conducted the measure on a server with AMD EPYC 7282 16-Core Processor, RAM 64 GB, and GPU Nvidia Tesla V100S 32 GB. We consider reparameterization because even if the number of parameters and GFlops are roughly the same, the inference time is lower using it in the inference step, so we limit our consideration of these

Table 6: Comparison between CellViT and NuLite (ours) on a batch of 4 patches over two input shapes (256, 1024), in terms of the number of parameters, number of multiplications and additions, and estimated size GPU latency

Model	Encoder	# Parameters	shape	Multiply-Adds (G)	Estimated Total Size (MB)	Latency (ms)
CellViT	ViT-256	46,750,349	256	132,8913	1,859.98	72 ± 0.39
			1024	2,125,9402	26,953.06	1489.1 ± 64.97
	SAM-B	146,094,557	256	200,1459	2,578.66	95.54 ± 0.2
			1024	3,200,6049	31,184.34	1437.2 ± 3.48
	SAM-L	367,847,645	256	207,0680	4,050.09	150.64 ± 0.26
NuLite	SAM-H	699,741,149	1024	3,306,5378	37,980.70	1940.66 ± 1.69
	fastvit-t8	9,237,389	256	14,7031	603.84	33.34 ± 1.13
			1024	235,2490	9,108.12	295.56 ± 1
	fastvit-t12	17,157,469	256	26,1658	834.00	36.96 ± 0.24
			1024	418,6516	12,315.90	349.84 ± 0.97
	fastvit-s12	19,077,341	256	26,5697	851.64	35.7 ± 1.23
			1024	425,1140	12,482.97	353.52 ± 1.09
NuLite-Rep	fastvit_sa12	21,184,733	256	26,5727	860.87	35.96 ± 1.28
			1024	425,1318	12,503.99	357.3 ± 0.91
	fastvit_sa24	31,157,981	256	28,2645	1,020.77	49.94 ± 1.37
			1024	452,1683	14,464.82	418.86 ± 1.49
	fastvit_sa36	41,131,229	256	29,9562	1,180.67	66.32 ± 1.23
NuLite-Rep	fastvit_ma36	57,837,473	256	42,0835	14,366.89	480.48 ± 0.66
			1024	673,2023	19,523.35	74,64 ± 3.08
	fastvit_t8	9,210,269	256	14,7005	564.85	25.8 ± 0.6
			1024	235,2077	8,485.20	278.72 ± 1.23
	fastvit_t12	17,116,701	256	26,1623	777.81	26.84 ± 0.79
NuLite-Rep	fastvit_s12	19,036,573	256	418,5965	11,418.23	324.06 ± 1.09
			1024	26,5662	795.45	26.88 ± 0.73
	fastvit_sa12	21,153,181	256	425,0589	11,585.29	328.64 ± 0.63
			1024	26,5693	806.80	27.98 ± 0.9
	fastvit_sa24	31,109,149	256	28,2610	928.91	332.12 ± 0.87
NuLite-Rep	fastvit_sa36	41,065,117	256	29,9528	1,051.02	35.46 ± 1.33
			1024	479,1497	14,353.52	376.66 ± 1.16
	fastvit_ma36	57,758,965	256	42,0794	1,282.94	44.58 ± 1.6
			1024	673,1369	17,062.69	421.28 ± 1.33
						56.72 ± 1.84
						676.72 ± 1.19

results in this analysis. According to these results, we can note that in terms of GFLOPS, all versions of NuLite are significantly lower than CellViT; further, all NuLite sizes are lower than CellViT. In terms of parameters, CellViT with SAM as the backbone is really big compared with our model, but the version with ViT-256 is smaller than NuLite with FastViT-MA36 as the backbone. CellViT takes a longer GPU latency than our NuLite versions because the amount of multiplication and addition is smaller than all CellViT versions. Moreover, if we consider our worst NuLite GPU latency for each shape, namely using FastViT-MA36 without reparameterization, it is faster than the best case of CellViT, namely CellViT256; moreover, it is almost

two times faster with shape 1024x1024. Limiting the analysis only to selected NuLite, we compared than with CellViT256 and CellViT-SAM-H in terms of the parameters, GFLOPS, and GPU latency. Table 7 presents a comparative analysis of the GFLOPS and the number of parameters for the NuLite models against CellViT architectures, including CellViT-256 and CellViT-SAM-H. The values indicate how computationally intensive and parameter-rich the CellViT models are compared to the corresponding NuLite variants. For GFLOPS, the CellViT-256 model is approximately 4.4 to 5.1 times more intensive than NuLite models, while CellViT-SAM-H ranges from 7.2 to 8.2 times more. Regarding the number of parameters, CellViT-256 has 1.1 to 2.7 times more parameters, whereas CellViT-SAM-H exhibits a significantly larger increase, ranging from 17 to 40.8 times more than NuLite models.

Table 7: Comparison of GFLOPS and parameters for NuLite models highlighting the multiples of GFLOPS and the number of parameters across CellViT architectures.

Model	GFLOPS		# Parameters	
	CellViT-256	CellViT-SAM-H	CellViT-256	CellViT-SAM-H
NuLite-T	5.1x	8.2x	2.7x	40.8x
NuLite-M	4.7x	7.6x	2.2x	33x
NuLite-H	4.4x	7.2x	1.1x	17x

Table 8 compares the inference speedups of NuLite models relative to CellViT architectures, specifically CellViT-256 and CellViT-SAM-H, for different patch sizes (256x256 and 1024x1024 pixels). The values indicate how much faster the NuLite models perform than the CellViT models. For a 256x256 patch size, the NuLite-T model achieves a speedup of 2.7 times over CellViT-256 and 7.8 times over CellViT-SAM-H. The NuLite-M and NuLite-H models also demonstrate notable speed improvements, though to a lesser extent. For the larger patch size of 1024x1024 pixels, the speedup is even more pronounced; NuLite-T reaches a speedup of 4.6 times over CellViT-256 and 7.7 times over CellViT-SAM-H.

Table 8: Inference Speedups for NuLite models with patch size 256X256 pixel and overlap 64px and patch size 1024X1024 over and CellViT architectures.

Model	Patch size: 256 X 256		Patch size: 1024 X 1024	
	CellViT-256	CellViT-SAM-H	CellViT-256	CellViT-SAM-H
NuLite-T	2.7x	7.8x	4.6x	7.7x
NuLite-M	2x	5.9x	4x	6.6x
NuLite-H	1.6x	4.7x	3.5x	5.9x

Lastly, to prove that our models are lighter than CellViT but performing as well as it, Figure 4 shows a comparison between them in terms of mPQ and bPQ, each error bar is the average standard deviation over tissue, on the x-axis there are GFLOPS on log-scale. Analyzing this image, we can note that our models are less complex than CellViT variants, but the results are approximately the same.

This indicates that while NuLite models maintain a lower computational and parameter footprint, they are being compared to highly demanding SOTA architectures, emphasizing their efficiency. Furthermore, the consistent performance ad-

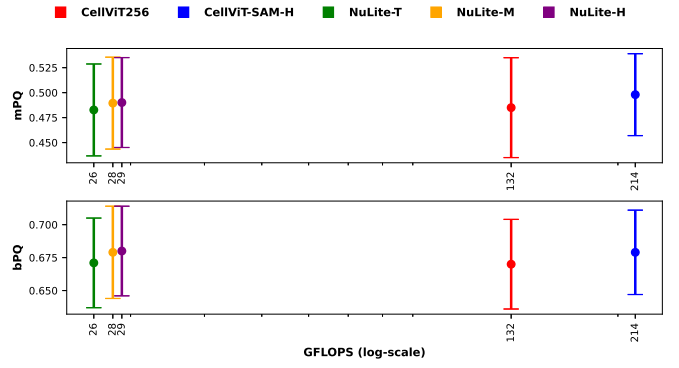


Figure 4: Comparison between CellViT256, CellViT-SAM-H, NuLite-T, NuLite-M, and NuLite-H in terms of multi-class and binary panoptic quality related to GFLOPS expressed in giga.

vantage highlights the efficiency of NuLite models in inference speed, particularly when dealing with larger image patches.

4.6. Results on others datasets

To understand the capability of generalization of NuLite, we used MoNuSeg, CoNSeP, and GlySAC datasets and compared the results against CellViT. In particular, we used GlySAC and CoNSeP to evaluate segmentation and classification performance. Instead, we used MoNuSeg to evaluate only segmentation performance because it does not provide nuclei type. As described in the dataset section, CoNSeP and GlySAC have different nuclei types of PanNuke, so we aligned them to compute multi-class metrics. All datasets contain tiles with shape 1000x1000, following the workflow introduced in [11], we resized them to 1024x1024 pixels. Lastly, we compared the results using the input shape of 256x256 pixels with an overlap of 64 pixels and 1024x1024 pixels. The authors in [11] proved that using an input shape of 1024x1024 does not negatively affect the results, but they analyzed what changes for multi-class metrics; in this section, we also analyze this aspect to understand if it is possible to use 1024x1024 pixels tile as input when we use NuLite on whole slide images. Here, we first analyze the binary metrics; table 9 contains the Detection Quality (DQ), Segmentation Quality (SQ), Panoptic Quality (PQ), Precision (P_d), Recall (R_d), and F1-score ($F_{1,d}$) for each dataset and inference configuration. First, we can confirm that using a tile of 1024x1024 as input is roughly equivalent to using a tile of 256x256 pixels with an overlap of 64 pixels.

NuLite consistently demonstrates competitive or superior performance compared to CellViT, particularly in precision and recall metrics. For instance, in the MoNuSeg dataset with 256x256 patches, NuLite-T achieves the highest recall (R_d) of 0.910, suggesting a strong ability to identify relevant instances. Similarly, NuLite-H delivers the best recall (0.725) and F1 score (0.774) for the CoNSeP dataset with smaller patches. Although CellViT-SAM-H shows slightly better overall scores on some datasets, NuLite variants are often close. NuLite-M even outperforms certain metrics, such as precision (P_d) in the GlySAC dataset. These findings suggest that NuLite, especially

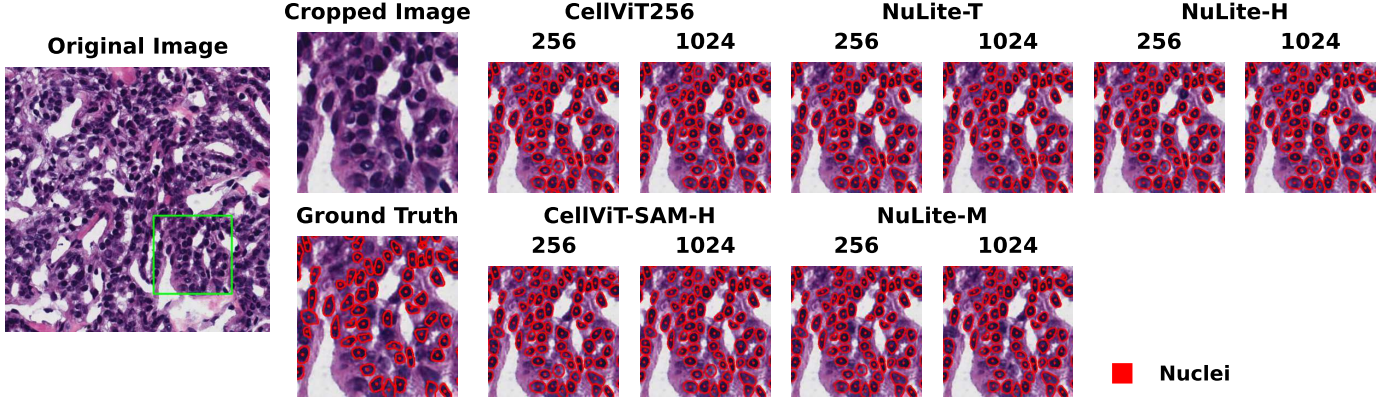


Figure 5: Segmentation masks generated by CellViT256, NuLite-T, NuLite-H, CellViT-SAM-H, and NuLite-M models on a histological image of tissue from the MoNuSeg dataset. Models were evaluated at 256x256 and 1024x1024 resolutions. Masks highlight nuclei.

Table 9: Comparison of CellViT, CellViT-SAM-H, and NuLite models (NuLite-T, NuLite-M, NuLite-H) across MoNuSeg, CoNSeP, and GlySAC datasets. Metrics include Detection Quality (DQ), Segmentation Quality (SQ), Panoptic Quality (PQ), and detection precision (P_d), recall (R_d), and F1-score ($F_{1,d}$) for patch sizes of 256x256 px and 1024x1024 px. The best results are highlighted in bold, with the second-best in underlined text.

Model	Patch-Size: 256 x 256 px - Overlap: 64 px						Patch-Size: 1024x1024 px						
	DQ	SQ	PQ	P_d	R_d	$F_{1,d}$	DQ	SQ	PQ	P_d	R_d	$F_{1,d}$	
MoNuSeg	CellViT-256	0.861	0.771	0.664	0.830	0.869	0.848	0.868	0.771	0.670	0.839	0.859	0.848
	CellViT-SAM-H	0.869	0.775	0.674	<u>0.850</u>	0.886	0.867	0.872	0.778	0.678	0.855	<u>0.893</u>	0.873
	NuLite-T	0.864	0.772	0.668	<u>0.846</u>	0.910	0.876	0.862	0.771	0.665	0.836	0.909	0.870
	NuLite-M	<u>0.865</u>	<u>0.774</u>	<u>0.670</u>	0.854	<u>0.896</u>	<u>0.873</u>	0.863	<u>0.775</u>	0.669	<u>0.851</u>	0.874	0.862
	NuLite-H	0.859	0.773	0.665	0.821	0.878	0.848	0.861	0.774	0.667	0.836	0.871	0.853
CoNSeP	CellViT-256	0.668	0.757	0.507	0.779	0.696	0.731	0.665	0.759	0.507	0.780	0.712	0.740
	CellViT-SAM-H	0.706	0.776	0.549	<u>0.817</u>	0.712	0.757	<u>0.714</u>	0.771	<u>0.552</u>	0.793	0.766	0.775
	NuLite-T	0.681	0.764	0.521	<u>0.815</u>	0.702	0.750	0.681	0.765	0.522	0.808	0.720	0.757
	NuLite-M	0.686	0.769	0.529	0.803	0.702	0.745	0.699	0.768	0.538	0.792	0.725	0.753
	NuLite-H	<u>0.702</u>	<u>0.773</u>	<u>0.544</u>	0.839	0.725	0.774	0.717	<u>0.770</u>	0.553	<u>0.796</u>	<u>0.745</u>	0.766
GlySAC	CellViT-256	0.744	0.735	0.552	0.843	0.813	0.825	0.743	0.735	0.552	0.845	<u>0.823</u>	0.830
	CellViT-SAM-H	0.746	0.740	0.558	<u>0.825</u>	<u>0.803</u>	0.811	<u>0.751</u>	<u>0.739</u>	0.560	0.846	0.811	0.826
	NuLite-T	<u>0.753</u>	0.743	<u>0.564</u>	0.834	<u>0.803</u>	0.816	0.748	<u>0.739</u>	0.558	0.826	0.825	0.822
	NuLite-M	0.754	0.743	0.565	0.834	0.813	<u>0.820</u>	0.755	0.743	0.566	0.843	0.816	0.825
	NuLite-H	0.750	<u>0.741</u>	0.562	<u>0.841</u>	0.802	0.818	0.747	0.743	<u>0.561</u>	0.859	0.804	0.828

its medium and high variants, can match or surpass the performance of the current state-of-the-art model, CellViT, in specific scenarios. Concerning binary results, we also show a visual example in Figure 5; in particular, it contains a tile of an image of the MoNuSeg date and an inference example of each analyzed model and each inference configuration setting.

Concerning the CoNSeP multi-class setting, we followed the alignment as shown in [29]; the Neoplastic class includes PanNuke’s neoplastic and CoNSeP’s dysplastic/malignant epithelial; the Inflammatory class encompasses PanNuke’s inflammatory and CoNSeP’s inflammatory; the Epithelial class consists of PanNuke’s epithelial and CoNSeP’s healthy epithelial; finally, the Miscellaneous class incorporates PanNuke’s dead and connective tissues alongside CoNSeP’s other types, which include fibroblast, muscle, and endothelial tissues.

Table 10 reports the results for CoNSeP multi-class comparing CellViT variants and the proposed NuLite variants across multiple tissue classes: Neoplastic, Epithelial, Inflammatory,

and Miscellaneous. Each model performance is evaluated using the two configuration settings described above, with metrics such as DQ (Dice Quality), SQ (Segmentation Quality), PQ (Panoptic Quality), Precision (P_d), Recall (R_d), and F1-score ($F_{1,d}$) reported for each class.

For patch size 256x256 pixels with 64-pixel overlap, the NuLite-H model demonstrates competitive performance, tying for the top score in the Neoplastic category (0.55) and performing strongly across other categories. CellViT-SAM-H generally leads in this setting, indicating its effectiveness with smaller image patches. However, the NuLite models show notable strengths in specific categories, highlighting their robustness and versatility. For patch size 1024x1024 pixels, NuLite models, particularly NuLite-H, show significant improvement and often outperform CellViT models. Notably, NuLite-H achieves the highest PQ scores in the Neoplastic category (0.58) and ties for the highest in the Miscellaneous category (0.44).

Regarding $F_{1,d}$ scores, NuLite-H consistently excels, partic-

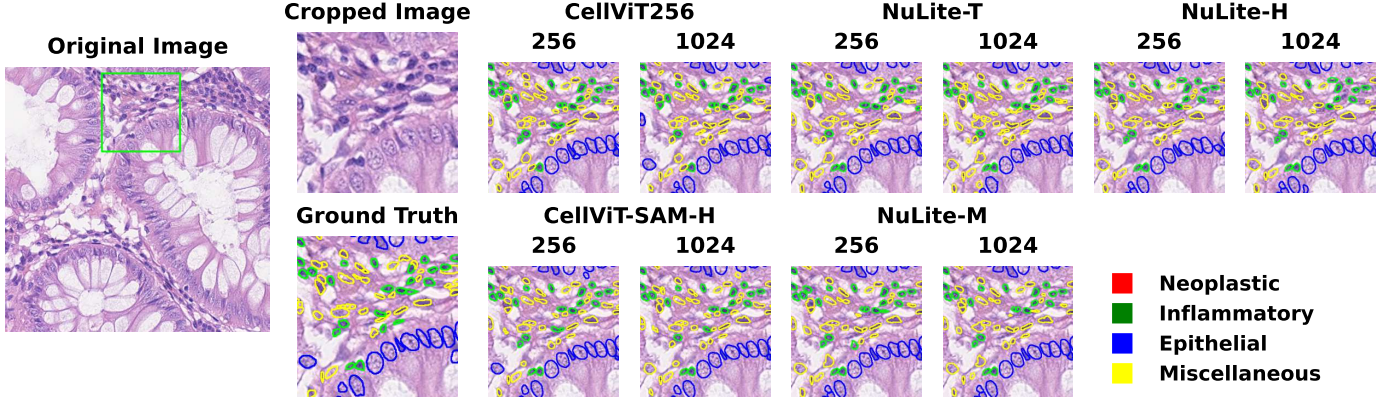


Figure 6: Segmentation masks generated by CellViT256, NuLite-T, NuLite-H, CellViT-SAM-H, and NuLite-M models on a histological image of epithelial tissue from the CoNSeP dataset. Models were evaluated at 256x256 and 1024x1024 resolutions. Masks highlight neoplastic, inflammatory, epithelial, and miscellaneous regions.

Table 10: Performance of CellViT-256, CellViT-SAM-H, NuLite-T, NuLite-M, and NuLite-H on the CoNSeP dataset across Neoplastic, Epithelial, Inflammatory, and Miscellaneous nuclei type with two patch sizes (256x256 px and 1024x1024 px). Metrics include Detection Quality (DQ), Segmentation Quality (SQ), and Panoptic Quality (PQ), along with detection precision (P_d), recall (R_d), and F1-score ($F_{1,d}$). The best results are highlighted in bold, and the second-best results are underlined.

Model	Patch-Size: 256 x 256 px - Overlap: 64												Patch-Size: 1024 x 1024 px											
	Neoplastic			Epithelial			Inflammatory			Miscellaneous			Neoplastic			Epithelial			Inflammatory			Miscellaneous		
	DQ	SQ	PQ	DQ	SQ	PQ	DQ	SQ	PQ	DQ	SQ	PQ	DQ	SQ	PQ	DQ	SQ	PQ	DQ	SQ	PQ	DQ	SQ	PQ
CellViT-256	0.53	0.66	0.4	0.69	0.77	0.53	0.66	0.8	<u>0.53</u>	0.52	0.73	0.38	0.52	<u>0.66</u>	0.39	0.64	0.77	0.49	0.61	0.82	0.5	0.48	0.68	0.35
CellViT-SAM-H	0.56	0.68	0.44	0.77	0.79	0.61	0.63	0.83	0.52	0.56	0.75	0.42	0.56	0.67	<u>0.44</u>	0.76	0.79	0.6	0.66	0.82	0.55	<u>0.58</u>	0.75	0.44
NuLite-T	0.56	0.67	0.43	0.74	0.79	0.58	0.65	0.82	0.53	<u>0.55</u>	0.74	0.4	0.57	0.67	<u>0.44</u>	0.75	0.78	<u>0.59</u>	0.63	0.8	0.52	0.55	0.74	0.41
NuLite-M	<u>0.55</u>	0.66	0.41	0.73	<u>0.78</u>	0.57	0.67	<u>0.82</u>	0.55	<u>0.55</u>	0.74	0.41	0.57	0.67	0.43	0.75	0.78	0.58	0.64	0.76	0.52	0.56	<u>0.74</u>	<u>0.41</u>
NuLite-H	0.55	0.67	0.42	0.77	0.78	0.6	0.62	0.77	0.51	<u>0.55</u>	0.74	0.41	0.58	0.67	0.45	0.77	0.78	0.6	0.65	0.77	<u>0.53</u>	0.59	0.75	0.44
	P_d	R_d	$F_{1,d}$	P_d	R_d	$F_{1,d}$	P_d	R_d	$F_{1,d}$	P_d	R_d	$F_{1,d}$	P_d	R_d	$F_{1,d}$	P_d	R_d	$F_{1,d}$	P_d	R_d	$F_{1,d}$	P_d	R_d	$F_{1,d}$
CellViT-256	0.59	0.57	0.57	0.54	0.63	0.58	0.6	0.64	0.56	0.62	0.51	0.55	0.53	0.57	0.55	0.5	0.71	0.58	0.61	0.52	0.52	0.61	0.46	0.51
CellViT-SAM-H	0.64	0.58	<u>0.6</u>	0.62	0.66	0.64	0.6	0.64	0.57	<u>0.67</u>	0.52	0.58	0.56	0.62	<u>0.59</u>	0.69	0.78	0.73	0.61	0.58	<u>0.56</u>	<u>0.66</u>	0.57	0.6
NuLite-T	0.62	<u>0.59</u>	<u>0.6</u>	0.62	0.65	0.64	0.63	0.57	0.58	0.66	0.5	0.56	0.59	0.58	0.58	<u>0.66</u>	<u>0.71</u>	<u>0.69</u>	0.6	<u>0.57</u>	<u>0.55</u>	<u>0.66</u>	0.52	0.57
NuLite-M	0.6	0.57	0.58	<u>0.66</u>	0.67	<u>0.66</u>	<u>0.65</u>	<u>0.59</u>	<u>0.59</u>	0.68	0.5	0.57	0.63	<u>0.61</u>	0.62	0.64	0.68	0.66	0.64	0.52	<u>0.56</u>	0.72	<u>0.57</u>	<u>0.59</u>
NuLite-H	0.66	0.61	<u>0.63</u>	0.68	<u>0.66</u>	0.67	0.67	0.58	<u>0.61</u>	0.68	<u>0.53</u>	0.59	<u>0.62</u>	<u>0.62</u>	0.63	0.67	0.65	0.65	0.56	0.59	0.65	<u>0.55</u>	<u>0.59</u>	

ularly with larger patch sizes achieving top scores in the Neoplastic (0.62), Epithelial (0.67), and Miscellaneous (0.59) nuclei type. This indicates that NuLite-H captures high precision and maintains strong recall, which is essential for accurate and reliable classification. The performance of NuLite-H in larger patches is particularly noteworthy, as it highlights the ability of the model to integrate broader contextual information, which is critical in complex image analysis tasks such as histopathology.

Furthermore, Figure 6 shows an inference example for each analyzed model highlighting a tile of an image of the CoNSeP dataset, where we can note that NuLite-H outputs the best visual result.

Concerning the results on GlySAC, we aligned the nuclei types as follows: the Epithelial class of GlySAC with Neoplastic and Epithelial of PanNuke, the Inflammatory class perfectly match, and the other class of PanNuke with the miscellaneous class of GlySAC. The results in Table 11 highlight the performance differences between NuLite variants and CellViT. The key metrics evaluated are Detection Quality (DQ), Segmentation Quality (SQ), Panoptic Quality (PQ), Precision, Recall, and F1 score for each nucleus type.

For epithelial nuclei, NuLite-H and CellViT-SAM-H exhibit similar high performance with Panoptic Quality (PQ) values of 0.42-0.43 at the 256x256 px patch size. At the larger

1024x1024 px input size, NuLite-H slightly outperforms with a PQ of 0.42, while NuLite-M and CellViT models are closely aligned. Regarding inflammatory nuclei, NuLite-M achieves the highest PQ score of 0.40 for 1024x1024 px patches, indicating superior performance. NuLite-H and CellViT-SAM-H also show strong results with PQ values around 0.39-0.41, demonstrating that NuLite effectively handles inflammatory cell segmentation, though the differences with CellViT are minimal. For miscellaneous nuclei, NuLite-M stands out with the highest PQ of 0.24 at the 1024x1024 px patch size, suggesting better segmentation performance in this challenging category. The advantage is less pronounced at the 256x256 px patch size, but NuLite still performs competitively. Furthermore, NuLite-H demonstrates strong performance in F1 scores, particularly in the 1024x1024 px input size, where it achieves the highest scores across most categories. This model reaches an F1 score of 0.50 for epithelial cells, indicating an effective balance between precision and recall. NuLite-T achieves a high recall value of 0.58 for epithelial cells with the 256x256 px patch size, indicating its effectiveness in identifying a larger proportion of relevant instances. However, this increased sensitivity may come at the cost of precision. Lastly, Figure 7 shows an inference example on GlySAC, where we can observe that NuLite-H achieves good results compared to ground truth.

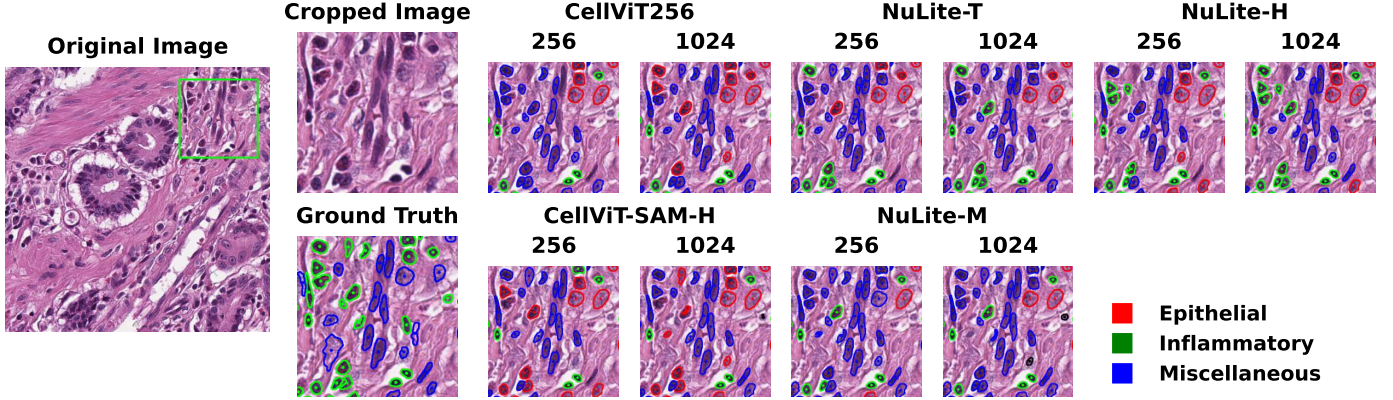


Figure 7: Comparison on different CellViT256, NuLite-T, NuLite-H, CellViT-SAM-H, and NuLite-M on an image from GlySAC dataset. Models are evaluated at different resolutions (256, 1024) and compared to ground truth. Segmentation masks highlight epithelial, inflammatory, and miscellaneous regions.

Table 11: Performance metrics for CellViT-256, CellViT-SAM-H, NuLite-T, NuLite-M, and NuLite-H on the GlySAC dataset. Metrics are provided for different patch sizes (256x256 px and 1024x1024 px) and include Detection Quality (DQ), Segmentation Quality (SQ), and Panoptic Quality (PQ) for Epithelial, Inflammatory, and Miscellaneous categories. Detection precision (P_d), recall (R_d), and F1-score ($F_{1,d}$) are also shown. The highest values are highlighted in bold, and the second-highest values are underlined.

Model	Patch-Size: 256 x 256 px - Overlap: 64									Patch-Size: 1024 x 1024 px								
	Epithelial			Inflammatory			Miscellaneous			Epithelial			Inflammatory			Miscellaneous		
	DQ	SQ	PQ	DQ	SQ	PQ	DQ	SQ	PQ	DQ	SQ	PQ	DQ	SQ	PQ	DQ	SQ	PQ
CellViT-256	0.53	<u>0.72</u>	0.40	0.54	0.73	<u>0.40</u>	0.31	0.70	<u>0.22</u>	0.51	0.73	0.39	0.50	0.71	0.38	0.29	0.69	0.20
CellViT-SAM-H	0.56	0.76	<u>0.43</u>	<u>0.55</u>	0.74	0.42	<u>0.32</u>	0.70	0.23	<u>0.54</u>	0.77	<u>0.41</u>	0.54	0.74	0.41	<u>0.31</u>	0.69	<u>0.22</u>
NuLite-T	<u>0.55</u>	0.76	0.42	0.49	0.71	0.38	0.29	0.70	0.21	0.53	0.76	<u>0.41</u>	0.51	0.71	0.38	0.30	0.70	<u>0.22</u>
NuLite-M	0.54	0.76	0.41	0.52	0.75	0.39	<u>0.31</u>	0.71	0.22	0.53	0.76	0.40	0.53	0.75	<u>0.40</u>	0.33	0.71	<u>0.24</u>
NuLite-H	0.56	0.76	0.42	0.51	<u>0.74</u>	0.39	<u>0.31</u>	0.70	<u>0.22</u>	0.55	0.76	0.42	0.51	0.74	0.39	0.31	0.71	0.22
	P_d	R_d	$F_{1,d}$	P_d	R_d	$F_{1,d}$	P_d	R_d	$F_{1,d}$	P_d	R_d	$F_{1,d}$	P_d	R_d	$F_{1,d}$	P_d	R_d	$F_{1,d}$
CellViT-256	<u>0.52</u>	0.49	0.47	<u>0.53</u>	0.53	0.45	0.32	0.33	0.29	0.47	0.49	0.45	0.54	0.45	0.41	0.31	0.33	0.27
CellViT-SAM-H	0.50	<u>0.53</u>	0.48	<u>0.55</u>	0.48	0.44	<u>0.37</u>	0.31	0.27	0.48	<u>0.53</u>	0.46	0.57	0.45	0.43	0.35	0.35	0.30
NuLite-T	0.45	0.58	0.47	<u>0.55</u>	0.38	0.40	<u>0.33</u>	0.30	0.27	0.49	<u>0.53</u>	0.48	0.53	0.40	0.40	0.31	<u>0.36</u>	0.28
NuLite-M	0.50	0.51	<u>0.47</u>	0.55	0.45	0.42	0.31	<u>0.35</u>	0.29	0.53	0.49	0.46	<u>0.55</u>	0.43	<u>0.42</u>	0.31	0.40	0.30
NuLite-H	<u>0.54</u>	0.52	0.48	<u>0.53</u>	0.41	0.41	<u>0.32</u>	0.37	0.30	<u>0.58</u>	0.56	0.50	0.51	<u>0.44</u>	0.42	0.34	0.33	0.29

5. Discussion

In this section, we draw back the discussion of our experimental results. According to the training results in PanNuke, we can assert that our model is equivalent to CellViT-SAM-H and, almost in every analyzed case, better than CellViT-256 in terms of each analyzed metric. Still, we can also assert that our model is less complex than CellViT, especially considering the version with SAM-H with backbone. In fact, the complexity and time inference analysis proved that our model is up about 8 times faster, with parameters up to 40 times lower. Moreover, the comparative analysis of NuLite and CellViT across MoNuSeg, CoNSeP, and GlySAC datasets highlights several key findings related to model performance and generalization capabilities in medical image segmentation tasks. The NuLite models, especially NuLite-H, demonstrate strengths in handling larger input sizes, showing superior or competitive performance against the state-of-the-art CellViT models. This makes them particularly valuable for applications requiring extensive spatial analysis, such as large-scale tissue image segmentation. The consistently high scores across multiple metrics and categories underscore the versatility and robustness of NuLite-H.

positioning it as a significant advancement in the field. One notable aspect of the study was comparing performance using different patch sizes (256x256 pixels with 64-pixel overlap vs. 1024x1024 pixels). The results demonstrate that using larger patches (1024x1024 pixels) does not negatively impact the performance and may even slightly improve it in some cases. This is consistent with the findings of [11], which suggest that larger patch sizes can maintain or enhance the accuracy of multi-class metrics without compromising the ability of the model to delineate fine details. The slight performance variations between the two patch sizes across different models indicate that larger patches can be effectively utilized in NuLite and CellViT models, potentially simplifying the pre-processing pipeline and reducing computational overhead. The performance metrics across MoNuSeg, CoNSeP, and GlySAC datasets indicate that CellViT and NuLite are robust in handling diverse data types. However, the NuLite models, especially the medium (NuLite-M) and high (NuLite-H) variants, consistently show competitive or superior performance in several metrics compared to CellViT. Notably, in the MoNuSeg dataset, which focuses solely on segmentation, NuLite-T achieved the highest recall (R_d) of 0.910 with 256x256 patches, underscoring

its ability to detect relevant instances accurately. Similarly, NuLite-H demonstrated superior recall and F1 scores in the CoNSeP dataset, which involves more complex tissue classification tasks. The CoNSeP dataset, aligned with PanNuke nuclei types, provided a challenging environment for testing multi-class segmentation capabilities. Here, NuLite-H excelled, particularly in the Neoplastic and Miscellaneous categories, suggesting that the model is adept at handling various tissue types and complex boundaries. The strong performance in the Miscellaneous class, which includes a diverse range of tissues, further underscores the model's versatility. On the other hand, CellViT-SAM-H showed strong performance in the Epithelial class, indicating its efficacy in distinguishing epithelial tissues with high segmentation quality. The findings from this study have important implications for using these models in whole-slide imaging (WSI) applications. The ability to effectively use larger patches (1024x1024 pixels) could significantly streamline the process of analyzing large WSI data, reducing the need for extensive patch overlap and potentially accelerating the segmentation process. This is particularly relevant in clinical settings with critical time and computational resources.

6. Conclusion

In this work, we introduced NuLite, a fast and lightweight convolutional neural network for nuclei instance segmentation and classification in H&E stained histopathological images. With its U-Net architecture featuring three decoders for predicting nuclei, horizontal and vertical maps, and nuclei types, drawing inspiration from HoVer-Net, NuLite demonstrates considerable promise. Furthermore, we provided an extensive experimental setting on data not used for training, such as CoNSeP, MoNuSeg, and GlySAC, proving the ability to generalize our model. Therefore, our model demonstrated a state-of-the-art lightweight model in nuclei instance segmentation classification. In some scenarios, it outperforms also CellViT-SAM-H, which is the current SOTA but more complex and heavy than our NuLite. The study reveals that NuLite, especially its medium and high variants, performs on par with or even outperforms current state-of-the-art models like CellViT. Overall, NuLite represents a significant advancement in automated medical diagnostics, offering speed and accuracy that could enhance analysis efficiency in medical contexts. In future work, we will focus on the ability of our model to embed nuclei, as also shown in [11], and we will try to use its ability in cell-graph classification.

Acknowledgments

This study was partially supported by the PNRR MUR project PE0000013-FAIR. We acknowledge the CINECA award (project FVT-NSC) under the ISCRA initiative for the availability of high-performance computing resources and support.

References

- [1] K. B. Tran, J. J. Lang, K. Compton, R. Xu, A. R. Acheson, H. J. Henrikson, J. M. Kocarnik, L. Penberthy, A. Aali, Q. Abbas, et al., The global burden of cancer attributable to risk factors, 2010–19: a systematic analysis for the global burden of disease study 2019, *The Lancet* 400 (10352) (2022) 563–591.
- [2] A. H. Song, G. Jaume, D. F. Williamson, M. Y. Lu, A. Vaidya, T. R. Miller, F. Mahmood, Artificial intelligence for digital and computational pathology, *Nature Reviews Bioengineering* 1 (12) (2023) 930–949.
- [3] C. D. Bahadir, M. Omar, J. Rosenthal, L. Marchionni, B. Liechty, D. J. Pisapia, M. R. Sabuncu, Artificial intelligence applications in histopathology, *Nature Reviews Electrical Engineering* (2024) 1–16.
- [4] R. J. Chen, T. Ding, M. Y. Lu, D. F. Williamson, G. Jaume, A. H. Song, B. Chen, A. Zhang, D. Shao, M. Shaban, et al., Towards a general-purpose foundation model for computational pathology, *Nature Medicine* 30 (3) (2024) 850–862.
- [5] J. Van der Laak, G. Litjens, F. Ciompi, Deep learning in histopathology: the path to the clinic, *Nature medicine* 27 (5) (2021) 775–784.
- [6] A. Basu, P. Senapati, M. Deb, R. Rai, K. G. Dhal, A survey on recent trends in deep learning for nucleus segmentation from histopathology images, *Evolving Systems* 15 (1) (2024) 203–248.
- [7] O. Ronneberger, P. Fischer, T. Brox, U-net: Convolutional networks for biomedical image segmentation, in: *Medical image computing and computer-assisted intervention–MICCAI 2015: 18th international conference, Munich, Germany, October 5–9, 2015, proceedings, part III 18*, Springer, 2015, pp. 234–241.
- [8] K. He, X. Zhang, S. Ren, J. Sun, Deep residual learning for image recognition, in: *Proceedings of the IEEE conference on computer vision and pattern recognition*, 2016, pp. 770–778.
- [9] A. Dosovitskiy, L. Beyer, A. Kolesnikov, D. Weissenborn, X. Zhai, T. Unterthiner, M. Dehghani, M. Minderer, G. Heigold, S. Gelly, et al., An image is worth 16x16 words: Transformers for image recognition at scale, *arXiv preprint arXiv:2010.11929* (2020).
- [10] S. Graham, Q. D. Vu, S. E. A. Raza, A. Azam, Y. W. Tsang, J. T. Kwak, N. Rajpoot, Hover-net: Simultaneous segmentation and classification of nuclei in multi-tissue histology images, *Medical image analysis* 58 (2019) 101563.
- [11] F. Hörst, M. Rempe, L. Heine, C. Seibold, J. Keyl, G. Baldini, S. Ugurel, J. Siveke, B. Grünwald, J. Egger, et al., Cellvit: Vision transformers for precise cell segmentation and classification, *Medical Image Analysis* 94 (2024) 103143.
- [12] P. K. A. Vasu, J. Gabriel, J. Zhu, O. Tuzel, A. Ranjan, Fastvit: A fast hybrid vision transformer using structural reparameterization, in: *Proceedings of the IEEE/CVF International Conference on Computer Vision*, 2023, pp. 5785–5795.
- [13] J. Gamper, N. A. Koohbanani, K. Benes, S. Graham, M. Jahanifar, S. A. Khurram, A. Azam, K. Hewitt, N. Rajpoot, Pannuke dataset extension, insights and baselines, *arXiv preprint arXiv:2003.10778* (2020).
- [14] N. Kumar, R. Verma, D. Anand, Y. Zhou, O. F. Onder, E. Tsougenis, H. Chen, P.-A. Heng, J. Li, Z. Hu, et al., A multi-organ nucleus segmentation challenge, *IEEE transactions on medical imaging* 39 (5) (2019) 1380–1391.
- [15] T. N. Doan, B. Song, T. T. Vuong, K. Kim, J. T. Kwak, Sonnet: A self-guided ordinal regression neural network for segmentation and classification of nuclei in large-scale multi-tissue histology images, *IEEE Journal of Biomedical and Health Informatics* 26 (7) (2022) 3218–3228.
- [16] N. Malpica, C. O. De Solórzano, J. J. Vaquero, A. Santos, I. Vallcorba, J. M. García-Sagredo, F. Del Pozo, Applying watershed algorithms to the segmentation of clustered nuclei, *Cytometry: The Journal of the International Society for Analytical Cytology* 28 (4) (1997) 289–297.
- [17] X. Yang, H. Li, X. Zhou, Nuclei segmentation using marker-controlled watershed, tracking using mean-shift, and kalman filter in time-lapse microscopy, *IEEE Transactions on Circuits and Systems I: Regular Papers* 53 (11) (2006) 2405–2414.
- [18] J. Cheng, J. C. Rajapakse, et al., Segmentation of clustered nuclei with shape markers and marking function, *IEEE transactions on Biomedical Engineering* 56 (3) (2008) 741–748.
- [19] S. Wienert, D. Heim, K. Saeger, A. Stenzinger, M. Beil, P. Hufnagl, M. Dietel, C. Denkert, F. Klauschen, Detection and segmentation of cell nuclei in virtual microscopy images: a minimum-model approach, *Scientific reports* 2 (1) (2012) 503.

[20] A. Tareef, Y. Song, H. Huang, D. Feng, M. Chen, Y. Wang, W. Cai, Multi-pass fast watershed for accurate segmentation of overlapping cervical cells, *IEEE transactions on medical imaging* 37 (9) (2018) 2044–2059.

[21] M. Liao, Y.-q. Zhao, X.-h. Li, P.-s. Dai, X.-w. Xu, J.-k. Zhang, B.-j. Zou, Automatic segmentation for cell images based on bottleneck detection and ellipse fitting, *Neurocomputing* 173 (2016) 615–622.

[22] S. Ali, A. Madabhushi, An integrated region-, boundary-, shape-based active contour for multiple object overlap resolution in histological imagery, *IEEE transactions on medical imaging* 31 (7) (2012) 1448–1460.

[23] M. Veta, P. J. Van Diest, R. Kornegoor, A. Huisman, M. A. Viergever, J. P. Pluim, Automatic nuclei segmentation in h&e stained breast cancer histopathology images, *PLoS one* 8 (7) (2013) e70221.

[24] Y. Song, E.-L. Tan, X. Jiang, J.-Z. Cheng, D. Ni, S. Chen, B. Lei, T. Wang, Accurate cervical cell segmentation from overlapping clumps in pap smear images, *IEEE transactions on medical imaging* 36 (1) (2016) 288–300.

[25] N. Alemi Koohbanani, M. Jahanifar, A. Gooya, N. Rajpoot, Nuclear instance segmentation using a proposal-free spatially aware deep learning framework, in: *Medical Image Computing and Computer Assisted Intervention–MICCAI 2019: 22nd International Conference, Shenzhen, China, October 13–17, 2019, Proceedings, Part I* 22, Springer, 2019, pp. 622–630.

[26] K. He, G. Gkioxari, P. Dollár, R. Girshick, Mask r-cnn, in: *Proceedings of the IEEE international conference on computer vision*, 2017, pp. 2961–2969.

[27] S. E. A. Raza, L. Cheung, M. Shaban, S. Graham, D. Epstein, S. Pelen-garis, M. Khan, N. M. Rajpoot, Micro-net: A unified model for segmentation of various objects in microscopy images, *Medical image analysis* 52 (2019) 160–173.

[28] A. Hatamizadeh, Y. Tang, V. Nath, D. Yang, A. Myronenko, B. Landman, H. R. Roth, D. Xu, Unetr: Transformers for 3d medical image segmentation, in: *Proceedings of the IEEE/CVF winter conference on applications of computer vision*, 2022, pp. 574–584.

[29] C. Tommasino, C. Russo, A. M. Rinaldi, F. Ciompi, "hover-unet": Accelerating hovernet with unet-based multi-class nuclei segmentation via knowledge distillation, *arXiv preprint arXiv:2311.12553* (2023).

[30] M. Weigert, U. Schmidt, Nuclei instance segmentation and classification in histopathology images with stardist, in: *2022 IEEE International Symposium on Biomedical Imaging Challenges (ISBIC)*, IEEE, 2022, pp. 1–4.

[31] S. Chen, C. Ding, M. Liu, J. Cheng, D. Tao, Cpp-net: Context-aware polygon proposal network for nucleus segmentation, *IEEE Transactions on Image Processing* 32 (2023) 980–994.

[32] T. Ilyas, Z. I. Mannan, A. Khan, S. Azam, H. Kim, F. De Boer, Tsfd-net: Tissue specific feature distillation network for nuclei segmentation and classification, *Neural Networks* 151 (2022) 1–15.

[33] J. Chen, Y. Lu, Q. Yu, X. Luo, E. Adeli, Y. Wang, L. Lu, A. L. Yuille, Y. Zhou, Transunet: Transformers make strong encoders for medical image segmentation, *arXiv preprint arXiv:2102.04306* (2021).

[34] S. Zheng, J. Lu, H. Zhao, X. Zhu, Z. Luo, Y. Wang, Y. Fu, J. Feng, T. Xiang, P. H. Torr, et al., Rethinking semantic segmentation from a sequence-to-sequence perspective with transformers, in: *Proceedings of the IEEE/CVF conference on computer vision and pattern recognition*, 2021, pp. 6881–6890.

[35] M. Caron, H. Touvron, I. Misra, H. Jégou, J. Mairal, P. Bojanowski, A. Joulin, Emerging properties in self-supervised vision transformers, in: *Proceedings of the IEEE/CVF international conference on computer vision*, 2021, pp. 9650–9660.

[36] E. Xie, W. Wang, Z. Yu, A. Anandkumar, J. M. Alvarez, P. Luo, Segformer: Simple and efficient design for semantic segmentation with transformers, *Advances in neural information processing systems* 34 (2021) 12077–12090.